International Journal of Numerical Methods for Heat & Fluid Flow

4181

Casson-Williamson ternary hybrid nanofluid flow over a yawed cylinder with the impacts of multiple slips

Prabhugouda Mallanagouda Patil
Department of Mathematics, KLE Technological University, Hubli, India

Bharath Goudar
Department of Mathematics, Karnatak University Dharwad, Dharwad, India and Department of Mathematics, Global Academy of Technology, Bengaluru, India, and

Ebrahim Momoniat
Department of Mathematics and Applied Mathematics, University of Johannesburg, Johannesburg, South Africa

Received 2 March 2024
Revised 4 August 2024
Accepted 23 August 2024

Abstract

Purpose – Many industries use non-Newtonian ternary hybrid nanofluids (THNF) because of how well they control rheological and heat transport. This being the case, this paper aims to numerically study the Casson-Williamson THNF flow over a yawed cylinder, considering the effects of several slips and an inclined magnetic field. The THNF comprises Al_2O_3-TiO_2-SiO_2 nanoparticles because they improve heat transmission due to large thermal conductivity.

Design/methodology/approach – Applying suitable nonsimilarity variables transforms the coupled highly dimensional nonlinear partial differential equations (PDEs) into a system of nondimensional PDEs. To accomplish the goal of achieving the solution, an implicit finite difference approach is used in conjunction with Quasilinearization. With the assistance of a script written in MATLAB, the numerical results and the graphical representation of those solutions were ascertained.

Findings – As the Casson parameter β increases, there is an improvement in the velocity profiles in both chord and span orientations, while the gradients $Re^{1/2}C_f$, $Re^{1/2}\overline{C}_f$ reduce for the same variations of β. The velocities of Casson THNF are greater than those of Casson-Williamson THNF. Approximately, a 202% and a 32% ascension are remarked in the magnitudes of $Re^{1/2}C_f$ and $Re^{1/2}\overline{C}_f$ for Casson-Williamson THNF than the Casson THNF only. When velocity slip attribute S_1 jumps to 1 from 0.5, magnitude of both $F(\xi, \eta)$ and $Re^{1/2}C_f$ fell down and it is reflected to be 396% at $\xi = 1$, $Wi = 1$ and $\beta = 1$. An augmentation in thermal jump results in advanced fluid temperature and lower $Re^{-1/2}Nu$. In particular, about 159% of down drift is detected when S_2 taking 1.

Originality/value – There is no existing research on the effects of Casson-Williamson THNF flow over a yawed cylinder with multiple slips and an angled magnetic field, according to the literature.

Keywords Casson-Williamson fluid, Ternary hybrid nanofluid (THNF), Inclined magnetic field (IMF), Multiple slips, Implicit finite difference, Yawed cylinder

Paper type Research paper

Ebrahim Momoniat reports financial support was provided by National Research Foundation of South Africa under grant number 150070.

Conflict of interest/Competing interests: Authors have no conflict of interest.

International Journal of Numerical Methods for Heat & Fluid Flow
Vol. 34 No. 12, 2024
pp. 4181-4205
Emerald Publishing Limited
0961-5539
DOI 10.1108/HFF-03-2024-0176

Nomenclature

Wi = Williamson attribute;
G = nondimensional temperature;
Re = Reynolds number;
T = dimensional temperature;
Pr = Prandtl number;
S = Spanwise velocity (nondimensional);
Ri = Richardson number;
S_1 = velocity slip;
g = gravitational acceleration;
f = nondimensional stream function;
u, v, w = velocity components;
S_2 = thermal jump;
M = magnetic parameter;
C_p = specific heat capacity;
F = Chordwise velocity (nondimensional); and
Ec = Eckert number.

Greek signs

σ = electrical conductivity;
ψ = stream function;
α = angle of inclination of the magnetic field;
ξ, η = transformed variables;
ρ = density;
φ_i, $i = 1, 2, 3$ = nanoparticles volume fractions;
β^* = thermal expansion constant;
θ = yaw angle; and
ν = kinematic viscosity.

Acronyms

BHNF = binary hybrid nanofluid;
IMF = inclined magnetic field; and
THNF = ternary hybrid nanofluid.

Subscripts

f = Casson-Williamson fluid;
nf = Casson-Williamson nanofluid;
hnf = binary hybrid nanofluid;
$thnf$ = ternary hybrid nanofluid; and
w, ∞ = conditions at the wall and away from the wall.

1. Introduction

Various non-Newtonian fluid flows have long piqued the curiosity of scientists due to their potential utility in fields as diverse as biomedicine, industrial processes, polymers, food processing, clay combinations, lubricants, coal slurries, oil retrieval and more. Owing to the non-Newtonian fluids' versatility, a wide variety of non-Newtonian fluid models, including

tangent hyperbolic fluid models, Carreau, Eyring-Powell, Casson, Micropolar and Williamson, are available in the literature. To meet the requirements of industrial applications, researchers have integrated two distinct non-Newtonian fluid models such as Casson-Micropolar, Casson-Williamson and Casson-Carreau. In this research, we have focused our investigation on the Casson-Williamson fluid's flow properties. Only a handful of investigations have been conducted on the Casson-Williamson (Humane *et al.*, 2021; Abbas *et al.*, 2023; Kumar *et al.*, 2023a, 2023b; Yousef *et al.*, 2022; Akolade and Tijani, 2021; Bhuvaneswari *et al.*, 2019) fluid flow due to its complexity. In their prior work, Humane *et al.* (2021) investigated the effects of radiation and chemical reactions using Casson-Williamson nanofluids in conjunction with a porous stretching surface. The influence of ohmic dissipation on a porous slippery surface was studied by Abbas *et al.* (2023) by applying Casson-Williamson fluid flow. Kumar *et al.* (2023a, 2023b) introduced the magnetic dipole effect on a curved melting and stretching slippery sheet in an unsteady flow of Casson-Williamson nanofluid.

The industrial requirements are not solely dependent on the influence of non-Newtonian fluids. Dispersing the nanoparticles throughout the base fluid can accomplish this. Nanofluids are exceptional because of their tiny size and huge specific surface area, which allows them to carry more heat, provide smooth flow in transit, be durable and be homogeneous. Furthermore, hybrid nanofluids, composed of multiple types of nanoparticles, have notable utility in various industries. The idea of hybrid nanofluids with two components has been the subject of much research. Further, a "ternary hybrid nanofluid" (THNF) is a base fluid that contains three distinct kinds of nanoparticles, which are less critical in the literature (Manjunatha *et al.*, 2022; Nazir *et al.*, 2021; Oke, 2022). The proposed work's framework is based on the concept of THNF. Manjunatha *et al.* (2022) analyzed the heat transfer impact of SiO_2-TiO_2-Al_2O_3/H_2O THNF flow around a stretching sheet using the RKF-45 method. Nazir *et al.* (2021) looked at tangent hyperbolic THNF flow over a melting surface and discovered that ternary hybrid nanoparticles raise the surface force more than nanoparticles or hybrid nanoparticles by themselves.

Most of the aforementioned research assumes that the applied magnetic field acts perpendicular to the fluid's flow direction. Nonetheless, in real-world issues of practical concern, such as magnetic flow control, MHD power production, and other geophysical problems, the magnetic field may indirectly affect the fluid flow. It is well-known that a magnetic field slows down the flow, which in turn slows down the separation of the boundary layers. Hence, it is essential to consider what happens when the applied magnetic field isn't perpendicular to the fluid flow. So, we are thinking about the inclined magnetic field (IMF), where the field is not exactly perpendicular to the fluid flow. Hayat *et al.* (2017), Srinivasulu and Goud (2021), Abdelhafez *et al.* (2023), Arshad *et al.* (2023), etc., have worked on the impact of IMF over various geometries having different source terms.

Engineering applications that examine the flow across a yawed cylinder encompass drag cords, braced frames, cantilever suspensions, overhead conduits, raked marine files and many more. Also fundamental to the design of structural heat exchangers is the fluid's movement through a yawed cylinder. Flow dynamics around a yawed cylinder have been studied by Chiu and Lienhard (1967). The results show that the separation point is free from a yaw angle in the Spanwise orientation and will occur across the Chordwise orientation. In their numerical analysis, Thapa *et al.* (2014) focused on the flow along an inclined cylinder at the plane boundary. According to Gupta and Sarma's (1975) analysis of the unsteady flow along a yawed cylinder subjected to cross-flow, the corresponding friction coefficient in the Chordwise orientation falls as the non-similar variable takes on more significant values. According to recent work by Jenifer *et al.* (2021) on MHD flow through a yawed cylinder involving mass transfer, improving the MHD parameter can delay the separation. Hybrid nanofluid flow across a yawed cylinder has been studied by Khan *et al.* (2021). Their findings

show that although temperature decreases, the yaw angle increases velocity in span and Chordwise directions.

The aforementioned investigations all assumed that the boundary adheres to the no-slip criterion. Nevertheless, there may be instances where the no-slip boundary criterion is unsuitable. When fluids fail to cling to solid boundaries, a phenomenon known as slip velocity sets in. Smoothing surfaces and micro gadgets are just two of the numerous technological uses for fluids with slip velocity. Thermal slip is also a common occurrence in most manufacturing processes. Asmat *et al.* (2023) solved Stoke's second problem over a plate with multiple slips and radiation. The impact of multiple slips on an inclined MHD bioconvective flow along a sheet with Dufour–Soret effects was examined by Ahmad *et al.* (2023). One can find new research on the impact of several slips on the flow regime (Priyanka *et al.*, 2023; Kumar *et al.*, 2023a, 2023b; Nandeppanavar *et al.*, 2023).

There is no existing research on the effects of Casson-Williamson THNF flow over a yawed cylinder with multiple slips and an angled magnetic field, according to the literature. Further, the practical applications of the present study lie in wastewater treatment, polymer processing, heat transfer in nuclear reactors, fluid transport systems, drug delivery systems, etc. Therefore, it is essential to examine how these distinct factors impact the yawed cylinder in this particular scenario. This research aims to address the following key issues:

- comparison of Williamson and Casson-Williamson THNF;
- inclined MHD impact over the geometry;
- impact of THNF over two-component hybrid nanofluids and nanofluids;
- velocity and thermal slips influence over profiles and gradients; and
- influence of shapes of nanoparticles over energy transfer strength.

2. Mathematical formulation

A 2D flow of Casson-Williamson THNF around a yawed cylinder with radius R, yaw angle θ whose walls are maintained at constant temperature T_w is considered in a steady state, shown in Figure 1. The fluid exterior to the cylinder has a temperature of T_∞. Along the x-axis, we can see the flow direction, and the z-axis forms a right angle with it. The z-axis receives an external, inclined magnetic field having strength B_0. The u_∞ and w_∞ signify the free stream velocities in chord and span orientations. The u, v and w velocities run along the x, y and z directions. The momentum equation has been updated to account for fluctuations in density using Boussinesq's approximation (Gray and Giorgini, 1976; Patil, 2008; Patil *et al.*, 2010, 2013). Given these conditions, the equations that control the flow process are (Nazir *et al.*, 2021; Oke, 2022; Jenifer *et al.*, 2021; Schlichting and Gersten, 2000) as follows:

$$\frac{\partial u}{\partial x} + \frac{\partial v}{\partial y} = 0, \tag{1}$$

$$\left.\begin{aligned} u\frac{\partial u}{\partial x} + v\frac{\partial u}{\partial y} = u_e\frac{du_e}{dx} + \nu_{thnf}\left(1+\frac{1}{\beta}\right)\frac{\partial^2 u}{\partial y^2} + \sqrt{2}\,\Gamma\nu_{thnf}\frac{\partial u}{\partial y}\frac{\partial^2 u}{\partial y^2} - \frac{\sigma_{thnf}B_0^2}{\rho_{thnf}}(u-u_e)\sin^2(\alpha) \\ + g\beta^*_{thnf}(T-T_\infty)\sin(\theta), \end{aligned}\right\} \tag{2}$$

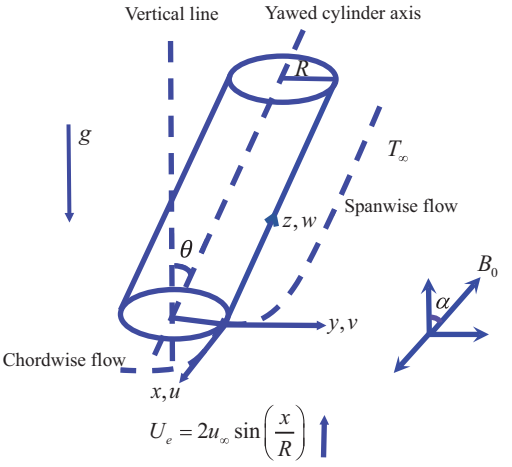

Source: Figure by authors

Figure 1. Flow illustration

$$u\frac{\partial w}{\partial x} + v\frac{\partial w}{\partial y} = \nu_{thnf}\left(1+\frac{1}{\beta}\right)\frac{\partial^2 w}{\partial y^2} + \sqrt{2}\,\Gamma\nu_{thnf}\frac{\partial w}{\partial y}\frac{\partial^2 w}{\partial y^2} - \frac{\sigma_{thnf}B_0^2}{\rho_{thnf}}w\sin^2(\alpha) + g\beta^*_{thnf}(T-T_\infty)\cos(\theta), \tag{3}$$

$$u\frac{\partial T}{\partial x} + v\frac{\partial T}{\partial y} = \frac{k_{thnf}}{(\rho C_p)_{thnf}}\frac{\partial^2 T}{\partial y^2} + \frac{\sigma_{thnf}B_0^2}{(\rho C_p)_{thnf}}(u_e-u)^2\sin^2(\alpha), \tag{4}$$

Boundary conditions (BCs):

$$\left.\begin{aligned} &\text{At } y=0: \quad u = s_1\frac{\partial u}{\partial y}; \quad v=0; \quad w=0; \quad T = T_w + s_2\frac{\partial T}{\partial y};\\ &\text{As } y\to\infty: \ u\to U_e = 2u_\infty\sin\left(\frac{x}{R}\right); \quad w\to w_e = w_\infty cos\,(\theta); \quad T\to T_\infty. \end{aligned}\right\} \tag{5}$$

Non-similar transformations (Jenifer *et al.*, 2021; Khan *et al.*, 2021):

$$\bar{x} = \int_0^x \frac{u_e}{u_\infty}\,d\left(\frac{x}{R}\right), \quad \eta = \left(\frac{Re}{2\bar{x}}\right)^{1/2}\frac{u_e}{u_\infty}\frac{y}{R}, \quad \psi(x,y) = u_\infty R\left(\frac{2\bar{x}}{Re}\right)^{1/2} f(\bar{x},\eta),$$

$$u = \frac{\partial\psi}{\partial y}, \quad v = -\frac{\partial\psi}{\partial x}, \quad G = \frac{T-T_\infty}{T_w-T_\infty}, \quad w = w_e S,$$

$$F = f_\eta,\ u = u_e F,\ v = -u_\infty \left(\frac{2\bar{x}}{Re}\right)^{1/2} \left\{ \frac{\sin\left(\frac{x}{R}\right)}{\bar{x}} f + 2\sin\left(\frac{x}{R}\right) f_{\bar{x}} - \eta \frac{\sin\left(\frac{x}{R}\right)}{\bar{x}} F + \eta \cot\left(\frac{x}{R}\right) F \right\}.$$

Nondimensional equations:

$$\left.\begin{aligned} a_1 \left[\left(1 + \frac{1}{\beta}\right) + Wi\, A_1(\bar{x}) F_\eta \right] F_{\eta\eta} + (f + 2\bar{x} f_{\bar{x}}) F_\eta - 2\bar{x}\, F F_{\bar{x}} + A_2(\bar{x})(1 - F^2) \\ - a_2 M^2 Re\, A_3(\bar{x}) \sin^2(\alpha)(F - 1) + a_3 A_4(\bar{x}) Ri \sin(\theta) G = 0, \end{aligned}\right\} \tag{6}$$

$$\left.\begin{aligned} a_1 \left[\left(1 + \frac{1}{\beta}\right) + Wi\, A_5(\bar{x}) \cot(\theta) S_\eta \right] S_{\eta\eta} + (f + 2\bar{x} f_{\bar{x}}) S_\eta - 2\bar{x}\, F S_{\bar{x}} \\ - a_2 M^2 Re\, A_3(\bar{x}) \sin^2(\alpha) S + a_3 A_3(\bar{x}) Ri \sin(\theta) G = 0, \end{aligned}\right\} \tag{7}$$

$$b_1 G_{\eta\eta} + Pr(f + 2\bar{x} f_{\bar{x}}) G_\eta - 2Pr\,\bar{x} F G_{\bar{x}} + Pr\, b_2 M^2 Re\, Ec\, \bar{x} \sin^2(\alpha)(F - 1)^2 = 0. \tag{8}$$

Nondimensional BCs:

$$\left.\begin{aligned} &\eta = 0: \quad F = \frac{1}{\sqrt{2}} A_5(\bar{x}) S_1 F_\eta; \quad S = 0; \quad G = 1 + \frac{1}{\sqrt{2}} A_5(\bar{x}) S_2 G_\eta; \\ &\eta \to \infty: \quad F \to 1; \quad S \to 1; \quad G \to 0. \end{aligned}\right\} \tag{9}$$

where, $a_1 = \frac{\nu_{thnf}}{\nu_f} or \frac{\mu_{thnf}/\mu_f}{\rho_{thnf}/\rho_f}$, $a_2 = \frac{\sigma_{thnf}/\sigma_f}{\rho_{thnf}/\rho_f}$, $a_3 = \frac{\beta^*_{thnf}}{\beta^*_f}$, $b_1 = \frac{k_{thnf}/k_f}{(\rho C_p)_{thnf}/(\rho C_p)_f}$,

$$b_2 = \frac{\sigma_{thnf}/\sigma_f}{(\rho C_p)_{thnf}/(\rho C_p)_f}, \quad A_1(\bar{x}) = \frac{4\sin^2\left(\frac{x}{R}\right)}{\sqrt{\bar{x}}}, \quad A_2(\bar{x}) = \frac{\bar{x}\cos\left(\frac{x}{R}\right)}{\sin^2\left(\frac{x}{R}\right)},$$

$$A_3(\bar{x}) = \frac{\bar{x}}{2\sin^2\left(\frac{x}{R}\right)}, \quad A_4(\bar{x}) = \frac{\bar{x}}{4\sin^3\left(\frac{x}{R}\right)}, \quad A_5(\bar{x}) = \frac{2\sin\left(\frac{x}{R}\right)}{\sqrt{\bar{x}}},$$

$$Pr = \frac{\mu_f C_{p_f}}{k_f}, \quad Wi = \Gamma u_\infty \left(\frac{u_\infty}{R\,\nu_f}\right)^{1/2}, \quad M^2 = \frac{\sigma_f B_0^2 \nu_f}{\rho_f u_\infty^2},$$

$$Re = \frac{u_\infty R}{\nu_f}, \quad Ri = \frac{g\beta^*_f (T_w - T_\infty) R}{u_\infty^2}, \quad Ec = \frac{u_\infty^2}{C_{p_f}(T_w - T_\infty)}.$$

Also, $f(\xi, \eta, \tau) = \int_0^\eta F_\eta \cdot d\eta + f_w$, here f_w vanishes as we have considered impermeable surface.

Nondimensional equations in ξ and η are obtained by converting $\bar{x}$ plane to ξ plane:
Let, $\xi = \frac{x}{R}$, we have $\bar{x} = 2\left(1 - \cos\left(\frac{x}{R}\right)\right)$

$$\Rightarrow \bar{x} = 2(1 - \cos(\xi)).$$

Consider $\overline{x}\frac{\partial}{\partial \overline{x}} = B(\xi)\frac{\partial}{\partial \xi}$, where $B(\xi) = \tan\left(\frac{\xi}{2}\right)$.

$\therefore A_1(\overline{x}),\ A_2(\overline{x}),\ A_3(\overline{x}),\ A_4(\overline{x}),\ A_5(\overline{x})$ in ξ can be expressed as follows:

$$A_1(\xi) = 4\sin(\xi)\cos\left(\frac{\xi}{2}\right),\quad A_2(\xi) = \frac{2\cos(\xi)}{(1+\cos(\xi))},\quad A_3(\xi) = \frac{1}{(1+\cos(\xi))},$$

$$A_4(\xi) = \frac{1}{2\sin(\xi)(1+\cos(\xi))},\quad A_5(\xi) = 2\cos\left(\frac{\xi}{2}\right).$$

Therefore, equations (6)–(8) in terms of ξ and η are as follows:

$$\left.\begin{aligned} &a_1\left[\left(1+\frac{1}{\beta}\right) + Wi\,A_1(\xi)F_\eta\right]F_{\eta\eta} + \left(f + 2B(\xi)f_\xi\right)F_\eta - 2B(\xi)FF_\xi + A_2(\xi)(1-F^2)\\ &- a_2M^2Re\,A_3(\xi)\sin^2(\alpha)(F-1) + a_3A_4(\xi)Ri\sin(\theta)G = 0, \end{aligned}\right\} \quad (10)$$

$$\left.\begin{aligned} &a_1\left[\left(1+\frac{1}{\beta}\right) + Wi\,A_5(\xi)\cot(\theta)S_\eta\right]S_{\eta\eta} + \left(f + 2B(\xi)f_\xi\right)S_\eta - 2B(\xi)FS_\xi\\ &- a_2M^2Re\,A_3(\xi)\sin^2(\alpha)S + a_3A_3(\xi)Ri\sin(\theta)G = 0, \end{aligned}\right\} \quad (11)$$

$$\left.\begin{aligned} &b_1G_{\eta\eta} + Pr\left(f + 2B(\xi)f_\xi\right)G_\eta - 2PrB(\xi)FG_\xi\\ &+ 2Pr\,b_2M^2Re\,Ec\,(1-\cos(\xi))\sin^2(\alpha)(F-1)^2 = 0. \end{aligned}\right\} \quad (12)$$

Nondimensional BCs:

$$\left.\begin{aligned} &\eta = 0: \quad F = \frac{1}{\sqrt{2}}A_5(\xi)S_1F_\eta; \quad S = 0; \quad G = 1 + \frac{1}{\sqrt{2}}A_5(\xi)S_2G_\eta;\\ &\eta \to \infty: \quad F \to 1; \quad S \to 1; \quad G \to 0. \end{aligned}\right\} \quad (13)$$

Gradients at the wall are as follows:
Chordwise skin-friction coefficient:

$$C_f = \frac{\tau_{w_x}}{\rho_f u_\infty^2} = \frac{\mu_{thnf}}{\rho_f u_\infty^2}\left\{\left(1+\frac{1}{\beta}\right)\left(\frac{\partial u}{\partial y}\right)_{y=0} + \frac{\Gamma}{\sqrt{2}}\left(\frac{\partial u}{\partial y}\right)^2_{y=0}\right\},$$

$$\Rightarrow Re^{1/2}C_f = \frac{\mu_{thnf}}{\mu_f}\sin(\xi)\cos\left(\frac{\xi}{2}\right)\left\{\sqrt{2}\left(1+\frac{1}{\beta}\right) + 4Wi\sin(\xi)\cos\left(\frac{\xi}{2}\right)F_\eta(\xi,0)\right\}F_\eta(\xi,0).$$

Spanwise skin-friction coefficient:

$$\overline{C}_f = \frac{\tau_{w_y}}{\rho_f u_\infty^2} = \frac{\mu_{thnf}}{\rho_f u_\infty^2}\left\{\left(1+\frac{1}{\beta}\right)\left(\frac{\partial w}{\partial y}\right)_{y=0} + \frac{\Gamma}{\sqrt{2}}\left(\frac{\partial w}{\partial y}\right)^2_{y=0}\right\},$$

$$\Rightarrow Re^{1/2}\overline{C}_f = \frac{\mu_{thnf}}{\mu_f}\cot(\theta)\cos\left(\frac{\xi}{2}\right)\left\{\sqrt{2}\left(1+\frac{1}{\beta}\right)+\frac{1}{\sqrt{2}}Wi\cot(\theta)\cos\left(\frac{\xi}{2}\right)S_\eta(\xi,0)\right\}S_\eta(\xi,0).$$

Heat transfer rate:

$$Nu = -\frac{k_{thnf}R\left(\frac{\partial T}{\partial y}\right)_{y=0}}{k_f(T_w - T_\infty)},$$

$$\Rightarrow Re^{-1/2}Nu = -\frac{k_{thnf}}{k_f}\sqrt{2}\cos\left(\frac{\xi}{2}\right)G_\eta(\xi,0).$$

3. Numerical method

The system has a pronounced nonlinear characteristic, as evidenced by equations (10)–(12). Once the Quasilinearization (Radbill and McCue, 1970; Bellman and Kalaba, 1965; Patil *et al.*, 2022; Patil *et al.*, 2019a, 2022) method has been applied, the linearized versions of equations (10) through (12) are given as follows:

$$F^{i+1}_{\eta\eta} + A^i_1 F^{i+1}_\eta + A^i_2 F^{i+1}_\xi + A^i_3 F^{i+1} + A^i_4 G^{i+1} = A^i_5, \tag{14}$$

$$S^{i+1}_{\eta\eta} + B^i_1 S^{i+1}_\eta + B^i_2 S^{i+1}_\xi + B^i_3 S^{i+1} + B^i_4 F^{i+1} + B^i_5 G^{i+1} = B^i_6, \tag{15}$$

$$G^{i+1}_{\eta\eta} + C^i_1 G^{i+1}_\eta + C^i_2 G^{i+1}_\xi + C^i_3 F^{i+1} = C^i_4, \tag{16}$$

BCs:

$$\left.\begin{array}{lll} F^{i+1}(\xi,\ 0) = F = \frac{1}{\sqrt{2}}A_5(\xi)S_1F_\eta, & S^{i+1}(\xi,\ 0) = 0, & G^{i+1}(\xi,\ 0) = 1 + \frac{1}{\sqrt{2}}A_5(\xi)S_2G_\eta, \quad \text{at } \eta = 0, \\ F^{i+1}(\xi,\ \eta_\infty) = 1, & S^{i+1}(\xi,\ \eta_\infty) = 1, & G^{i+1}(\xi,\ \eta_\infty) = 0, \quad \text{at } \eta = \eta_\infty. \end{array}\right\} \tag{17}$$

where i is known, and $i + 1$ is unknown regarding the iterative locations.

It anticipates that the equations (14) through (16) can be solved numerically through the execution of the implicit finite difference method (Inouye and Tate, 1974; Patil *et al.*, 2018, 2019b, 2023a, b). The analysis deployed a backward difference strategy for the x direction and a central difference scheme in the η direction. A fixed value of 0.01 is allocated for each step width $\Delta\eta$ and $\Delta\xi$. The MATLAB program is written for numerical computations and 2-D line plot in MATLAB is used for the graphical output. Convergence is achieved when the highest absolute variance between two subsequent iterations is below 10^{-8}. The computations are performed with 11th generation Intel Core i5 processor with SSD and 8 GB RAM. It is noticed that CPU time taken for the computation is around 10 s for different values of parameters.

The following are the coefficients of equations (14) to (16):

$$A^i_1 = dff\left(f + 2B(\xi)f_\xi\right) - df\Big\{2B(\xi)FF_\xi - A_2(\xi)(1-F^2) + a_2A_3(\xi)ReM^2\sin^2(\alpha)(F-1) - a_3A_4(\xi)Ri\sin(\theta)G\Big\},$$

$$A_2^i = -\frac{2}{Q_1}B(\xi)F, \quad A_3^i = -\frac{2}{Q_1}\left(B(\xi)F_\xi + A_2(\xi)F + \frac{a_2}{2}A_3(\xi)ReM^2\sin^2(\alpha)\right),$$

$$A_4^i = -\frac{a_3}{Q_1}A_4(\xi)Ri\sin(\theta),$$

$$A_5^i = A_1^i F_\eta + A_2^i F_\xi - \frac{1}{Q_1}\left(\left(f + 2B(\xi)f_\xi\right)F_\eta + A_2(\xi)\left(1+F^2\right) + a_2A_3(\xi)ReM^2\sin^2(\alpha)\right),$$

$$Q_1 = a_1\left[\left(1+\frac{1}{\beta}\right) + WiA_1(\xi)F_\eta\right], \quad df = -\frac{a_1WiA_1(\xi)}{Q_1^2}, \quad dff = \frac{a_1\left(1+\frac{1}{\beta}\right)}{Q_1^2},$$

$$B_1^i = dss\left(f + 2B(\xi)f_\xi\right) - ds\left(2B(\xi)FS_\xi + a_2M^2ReA_3(\xi)\sin^2(\alpha)S - a_3A_3(\xi)Ri\sin(\theta)G\right),$$

$$B_2^i = -\frac{2}{Q_2}B(\xi)F, \quad B_3^i = -\frac{a_2}{Q_2}M^2Re\,A_3(\xi)\sin^2(\alpha), \quad B_4^i = -\frac{2}{Q_2}B(\xi)S_\xi,$$

$$B_5^i = -\frac{a_3}{Q_2}A_3(\xi)Ri\sin(\theta), \quad B_6^i = B_1^iS_\eta - \frac{\left(f+2B(\xi)f_\xi\right)}{Q_2}S_\eta + B_2^iS_\xi,$$

$$Q_2 = a_1\left[\left(1+\frac{1}{\beta}\right) + WiA_5(\xi)\cot(\theta)S_\eta\right], \; ds = -\frac{a_1WiA_5(\xi)\cot(\theta)}{Q_2^2}, \; dss = \frac{a_1\left(1+\frac{1}{\beta}\right)}{Q_2^2},$$

$$C_1^i = \frac{Pr}{b_1}\left(f + 2B(\xi)f_\xi\right), \; C_2^i = -\frac{2}{b_1}Pr\,B(\xi)F,$$

$$C_3^i = -\frac{Pr}{b_1}\left(2B(\xi)G_\xi - 4b_2M^2Re\,Ec(1-\cos(\xi))\sin^2(\alpha)(F-1)\right),$$

$$C_4^i = C_2^iG_\xi + 2\frac{b_2}{b_1}Pr\,M^2Re\,Ec(1-\cos(\xi))\sin^2(\alpha)\left(F^2-1\right).$$

3.1 Convergence of a solution

Figure 2 shows the relationship between residue and iteration number. This plot shows how the residue changes as the number of iterations increases. It is used to analyze the convergence behaviour of the iterative method. Since the residue decreases and approaches a constant value (very much near to 0) as the number of iterations increases, the solution is converging. We have considered 1,000 iterations for the study.

3.2 Results validation

Table 1 offers instructive comparisons between the current results for $Re^{-1/2}Nu$ and those obtained by Takhar *et al.* (2000) and Roy and Anilkumar (2006). There is a significant degree of agreement between the results, as demonstrated by the comparison.

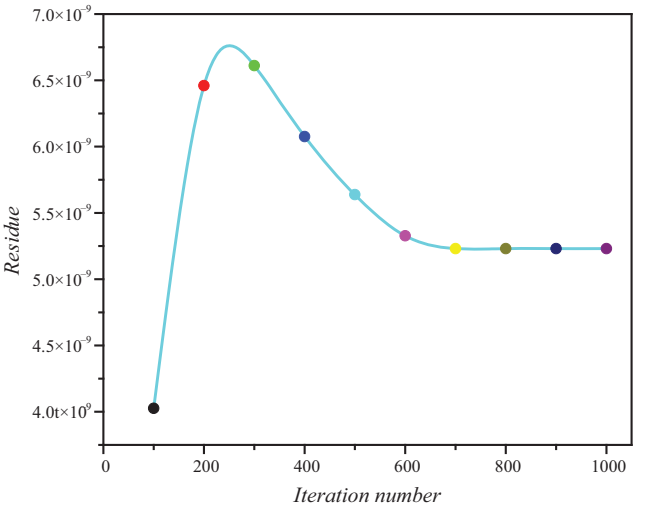

Source: Figure by authors

Figure 2. Residue against number of iterations

Table 1. Assessment of heat transfer efficiency

		Heat transfer efficiency ($Re^{-1/2}Nu$)		
ξ	Ri	Takhar *et al.* (2000)	Roy and Anilkumar (2006)	Our results
0	0	0.5854	0.5854	0.5852
0	1	0.8219	0.8220	0.8221
0	2	0.9302	0.9304	0.9306
1	0	0.8666	0.8666	0.8666
1	1	1.0617	1.0621	1.0622
1	2	1.1685	1.1688	1.1686

4. Results and discussion

The results of our investigation are presented in this section, which serves as an essential section. The physical outcomes for the Williamson attribute ($0 \le Wi \le 1$), Casson attribute ($0.5 \le \beta \le 2$), velocity slip ($0.5 \le S_1 \le 1.0$), thermal jump ($0.5 \le S_2 \le 1.0$), magnetic attribute ($0 \le M \le 3$), the inclination angle of the magnetic field ($30° \le \alpha \le 60°$), yaw angle ($15° \le \theta \le 60°$), nanoparticle volume fraction ($0 \le \varphi_i \le 0.02$) $i = 1, 2, 3$, nanoparticle shape factor ($3 \le s \le 16.1576$) regarding velocity profiles ($F(\xi, \eta)$, $S(\xi, \eta)$), surface drag coefficients $\left(Re^{1/2}C_f,\ Re^{1/2}\overline{C}_f\right)$ in both chord and Spanwise orientations and heat transmission ability ($Re^{-1/2}Nu$) are discussed. Table 2 presents the thermal characteristics of various nanoparticles that were taken into consideration.

Expressions of ternary hybrid nanoparticles' thermal features (Gul and Saeed, 2022)

Density:

$$\rho_{thnf} = (1-\varphi_1)\left[(1-\varphi_2)\left\{(1-\varphi_3)+\varphi_3\rho_3\right\}+\varphi_2\rho_2\right]+\varphi_1\rho_1$$

Dynamic viscosity:

Table 2. Nanoparticles' thermal properties

Properties	Al_2O_3	TiO_2	SiO_2	Water
$k(W/mK)$	40	8.9538	1.4	0.613
$\rho(kg/m^3)$	3970	4250	2200	997.1
$C_p(J/kgK)$	765	686.2	745	4179
$\beta^*(1/K) \times 10^{-5}$	0.85	0.9	0.9	21
$\sigma(\Omega m)^{-1}$	5.96×10^7	2.4×10^6	3.5×10^6	5.5×10^{-6}

Source: Benkhedda *et al.* (2018), Xu (2019) and Manjunatha *et al.* (2022)

$$\mu_{thnf} = \frac{\mu_f}{(1-\varphi_1)^{2.5}(1-\varphi_2)^{2.5}(1-\varphi_3)^{2.5}}$$

Thermal conductivity:

$$k_{thnf} = \frac{k_3 + 2k_{hnf} - (s-1)\varphi_3(k_{hnf} - k_3)}{k_3 + 2k_{hnf} + \varphi_2(k_{hnf} - k_3)} * k_{hnf},$$

where $k_{hnf} = \frac{k_2 + 2k_{nf} - (s-1)\varphi_1(k_{nf} - k_2)}{k_2 + 2k_{nf} + \varphi_1(k_{nf} - k_2)} * k_{nf}$:

$$k_{nf} = \frac{k_1 + 2k_f - (s-1)\varphi_1(k_f - k_1)}{k_1 + 2k_f + \varphi_1(k_f - k_1)} * k_f$$

Heat capacitance:

$$(\rho C_p)_{thnf} = (1-\varphi_1)\left[(1-\varphi_2)\left\{(1-\varphi_3) + \varphi_3(\rho C_p)_3\right\} + \varphi_2(\rho C_p)_2\right] + \varphi_1(\rho C_p)_1$$

Thermal expansion coefficient:

$$(\rho C_p)_{thnf} = (1-\varphi_1)\left[(1-\varphi_2)\left\{(1-\varphi_3) + \varphi_3(\rho\beta)_3\right\} + \varphi_2(\rho\beta)_2\right] + \varphi_1(\rho\beta)_1$$

Electrical conductivity:

$$\sigma_{thnf} = \frac{\sigma_3 + 2\sigma_{hnf} - 2\varphi_3(\sigma_{hnf} - \sigma_3)}{\sigma_3 + 2\sigma_{hnf} + \varphi_2(\sigma_{hnf} - \sigma_3)} * \sigma_{hnf},$$

where $\sigma_{hnf} = \frac{\sigma_2 + 2\sigma_{nf} - 2\varphi_1(\sigma_{nf} - \sigma_2)}{\sigma_2 + 2\sigma_{nf} + \varphi_1(\sigma_{nf} - \sigma_2)} * \sigma_{nf}$:

$$\sigma_{nf} = \frac{\sigma_1 + 2\sigma_f - 2\varphi_1(\sigma_f - \sigma_1)}{\sigma_1 + 2\sigma_f + \varphi_1(\sigma_f - \sigma_1)} * \sigma_f$$

4.1 Casson (β), Williamson (W_i), velocity slip (S_1) parameters effects

A correlation is shown in Figures 3–6 between the flow regulating parameters, such as Casson (β), Williamson (Wi), velocity slip (S_1) and the velocity profiles ($F(\xi, \eta)$, $S(\xi, \eta)$) and surface drag coefficients $\left(Re^{1/2}C_f,\ Re^{1/2}\overline{C}_f\right)$ in both chord and Spanwise orientations. As the Casson parameter increases, we see an improvement in the velocity profiles in both orientations while the gradients $Re^{1/2}C_f$, $Re^{1/2}\overline{C}_f$ reduce for the same variations of β. A decrement of about

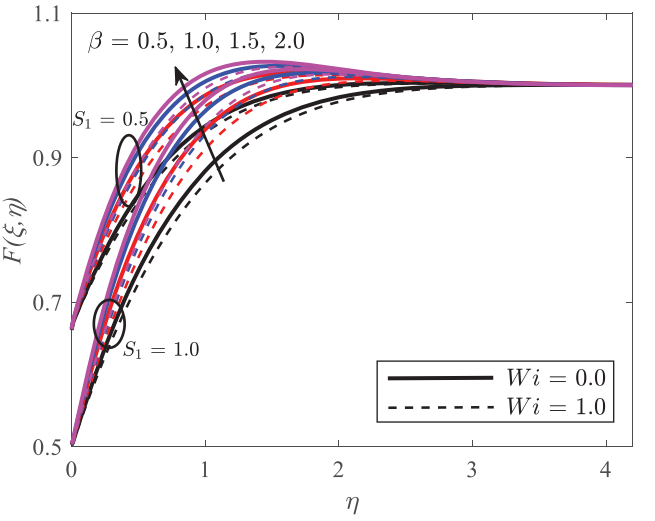

Source: Figure by authors

Figure 3. Impact of velocity slip (S_1), Casson parameter (β) and Williamson parameter (Wi) on the chordwise velocity profile

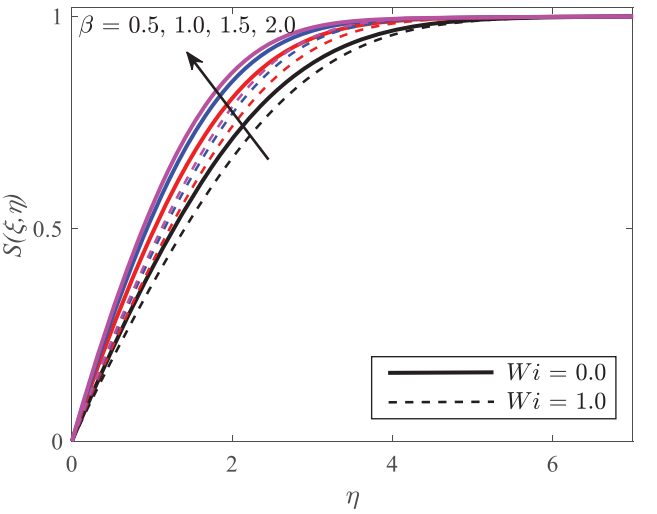

Source: Figure by authors

Figure 4. Impact of Casson parameter (β) and Williamson parameter (Wi) on the spanwise velocity profile

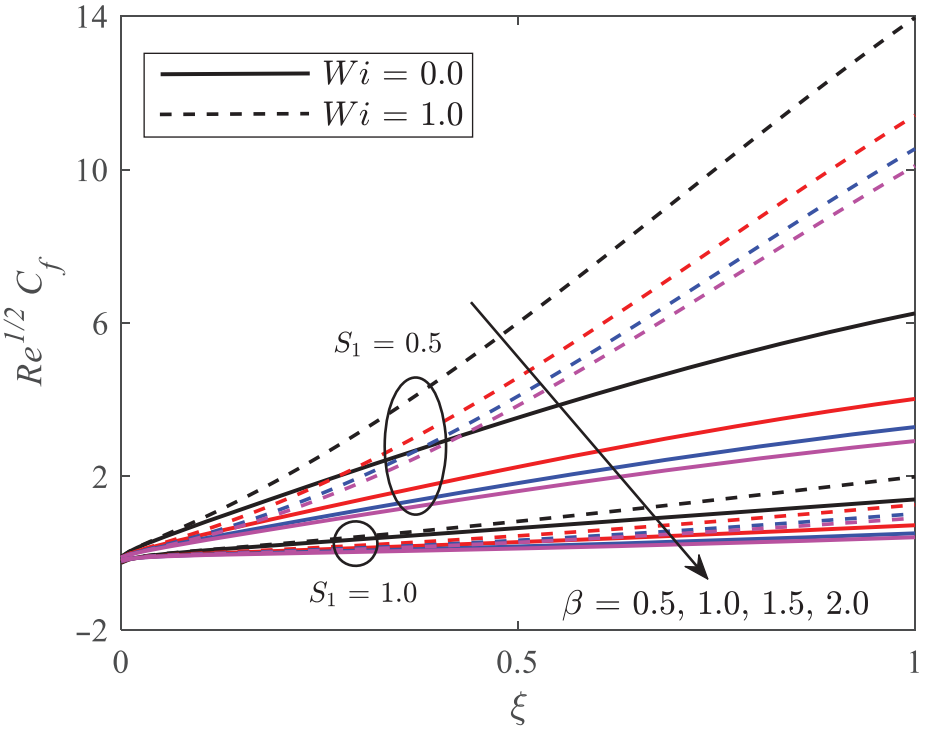

Source: Figure by authors

Figure 5. Impact of velocity slip (S_1), Casson parameter (β) and Williamson parameter (Wi) on the chordwise skin-friction coefficient

38% and 64% in $Re^{1/2}C_f$ and $Re^{1/2}\overline{C}_f$ is noted from Figures 4 and 5 at $\xi = 1$, $Wi = 1$ and $S_1 = 0.5$ for rising β from 0.5 to 2.0. The possible cause could be that the combined influence of yield stress and Casson viscosity determines the overall flow behaviour. A Casson fluid characterized by a substantial yield stress and a low Casson viscosity may demonstrate a prominent yield point, followed by a comparatively effortless flow once the yield stress threshold is exceeded. Conversely, a fluid with low threshold stress and high Casson viscosity may exhibit more effortless flow yet present increased resistance with higher shear rates.

Furthermore, Figures 3–6 confer the difference in the Casson THNF ($Wi = 0$) and Casson-Williamson THNF ($Wi = 1$) velocities and frictions in both orientations. The velocities of Casson THNF are observed to be greater than those of Casson-Williamson THNF. Additionally, the friction encountered on the surface of the yawed cylinder is higher when using Casson-Williamson THNF compared to using Casson THNF alone. In particular, approximately a 202% and a 32% ascension are remarked in the magnitudes of $Re^{1/2}C_f$ and $Re^{1/2}\overline{C}_f$ for Casson-Williamson THNF than the Casson THNF only at $\xi = 1$ and $\beta = 1$. This is a result of the differing viscosities of the two fluids. The viscosity of Casson THNF is lower than that of Casson-Williamson THNF. This lowers the flow's velocity, which boosts surface friction. Additionally, Figures 3 and 5 graphed the impression of velocity slip parameter (S_1)

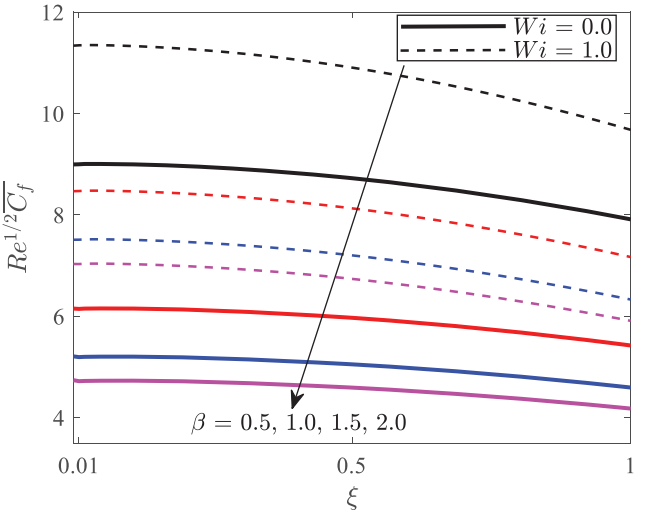

Source: Figure by authors

Figure 6. Impact of Casson parameter (β) and Williamson parameter (Wi) on the spanwise skin-friction coefficient

on $F(\xi, \eta)$ and $Re^{1/2}C_f$. When S_1 jumps to 1 from 0.5, magnitude of both $F(\xi, \eta)$ and $Re^{1/2}C_f$ fell down and it is reflected to be 396% at $\xi = 1$, $Wi = 1$ and $\beta = 1$. Because the slip velocity exerts a lesser influence on the fluid velocity, the slip velocity improves with larger values of S_1, which minimizes the fluid velocity and friction within the boundary layer.

4.2 Angle of inclination of the magnetic field, thermal jump and magnetic parameter effects

The influence of the applied inclined magnetic field (IMF) is observed through Figures 7–12, where the effect of both magnetic (M) and inclined angle attributes (α) are picturized. The chordwise velocity ($F(\xi, \eta)$) and temperature ($G(\xi, \eta)$) profiles and their corresponding gradients got the same fluctuations for varying M and α. *i.e.* rising variations of M and αadvance the $F(\xi, \eta)$, $G(\xi, \eta)$, energy transport ability ($Re^{-1/2}Nu$) and hinder the growth of friction along Spanwise orientation. Selectively, a decline of approximately 82% and 72% in $Re^{1/2}C_f$ and $Re^{1/2}\overline{C}_f$ are noted while M emerges from 0 to 2 and α from 30° to 60° at $\xi = 1$. If the fluid passing through the cylinder is conductive, an electric current can be induced by applying a magnetic field at an angle to the flow direction. As the induced electric current combines with the magnetic field, a Lorentz force is generated. As a result, it can alter the flow pattern such that the cylinder's surface experiences less drag or friction. In addition, M and α diminish $S(\xi, \eta)$ and $Re^{1/2}\overline{C}_f$ in Spanwise orientation. The $Re^{1/2}\overline{C}_f$ declines moderately about 42% for enhancing M from 0 to 3, and a significantly less 5% lessen is observed for rising α to 60° from 30^0. The limited influence of an inclined magnetic field on the Spanwise orientation is the reason behind this. Further, thermal jump (S_2) influence on $G(\xi, \eta)$ and $Re^{-1/2}Nu$ can be seen in Figures 9 and 12. An augmentation in thermal jump results in advanced fluid temperature and lower $Re^{-1/2}Nu$. In particular, about 159% of down drift is detected when S_2 taking 1.

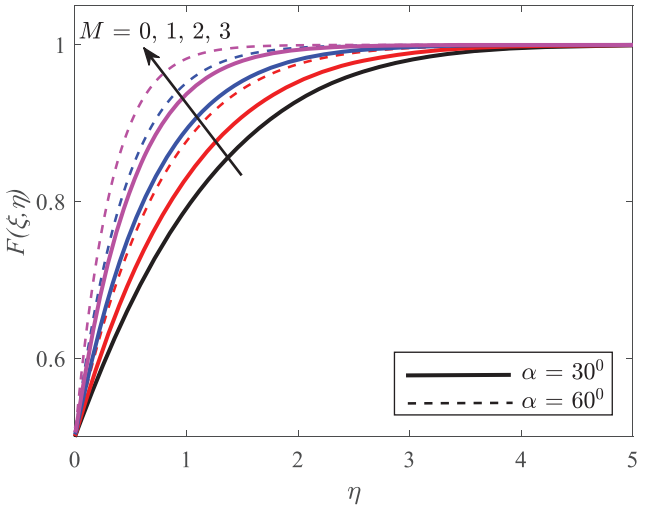

Source: Figure by authors

Figure 7. Impact of inclined magnetic field parameter (m) and angle of inclination (α) of the magnetic field on the chordwise velocity profile

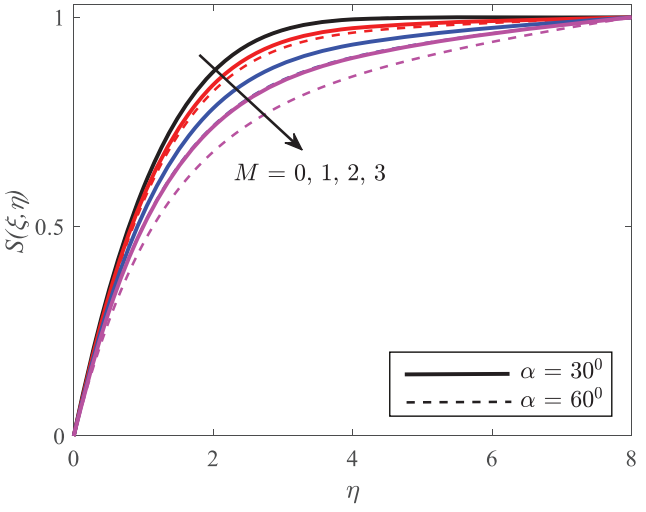

Source: Figure by authors

Figure 8. Impact of inclined magnetic field parameter (m) and angle of inclination (α) of the magnetic field on the Spanwise velocity profile

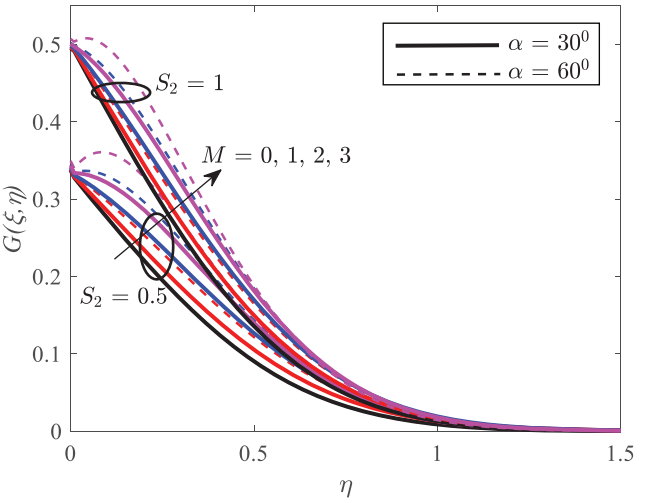

Source: Figure by authors

Figure 9. Impact of thermal jump (S_2), inclined magnetic field parameter (m) and angle of inclination (α) of the magnetic field on the temperature profile

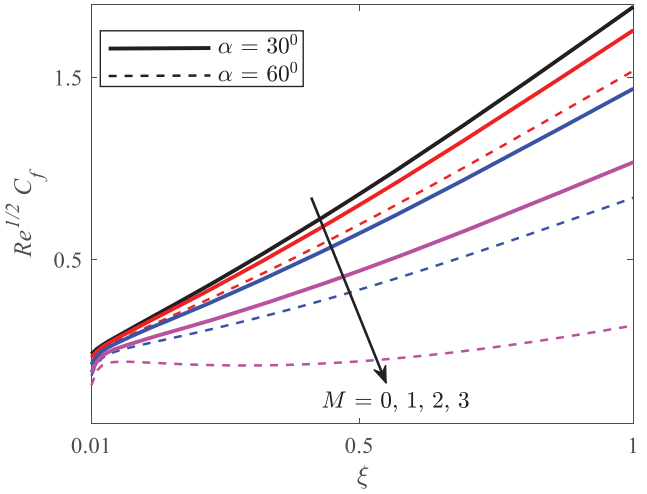

Source: Figure by authors

Figure 10. Impact of inclined magnetic field parameter (m) and angle of inclination (α) of the magnetic field on the chordwise skin-friction coefficient

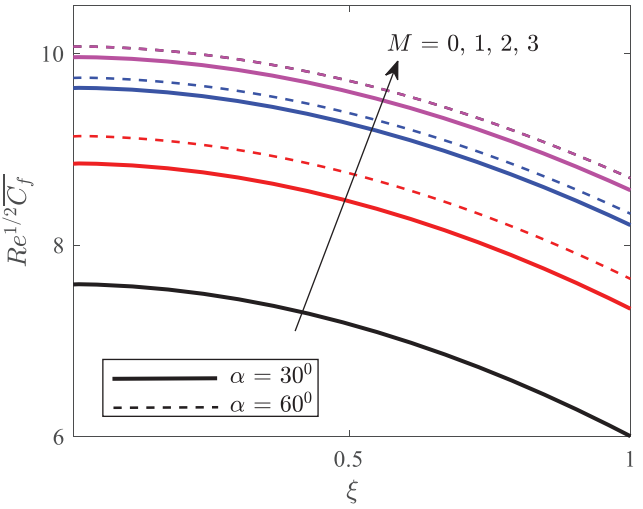

Source: Figure by authors

Figure 11. Impact of inclined magnetic field parameter (m) and angle of inclination (α) of the magnetic field on the spanwise skin-friction coefficient

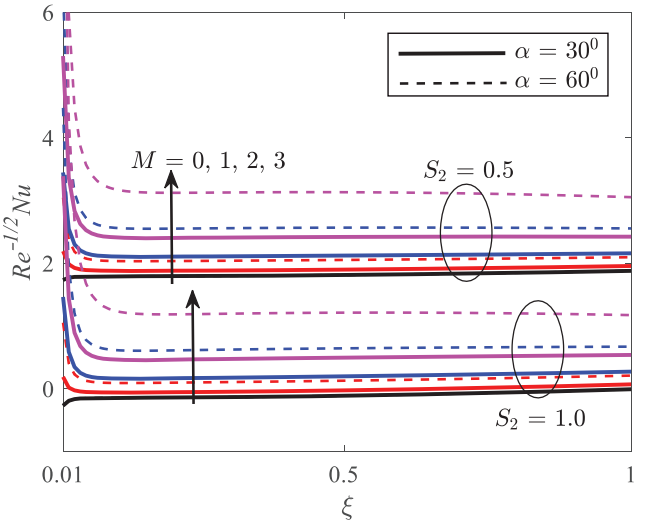

Source: Figure by authors

Figure 12. Impact of thermal jump (S_2), inclined magnetic field parameter (m) and angle of inclination (α) of the magnetic field on the heat transfer rate

4.3 Yaw angle and third component of ternary hybrid nanofluid effects

Figures 13–16 give an exposure to the implications of the yaw angle (θ) and discrepancy between binary (BHNF) and ternary hybrid nanofluids (THNF) on the chord and Spanwise velocities ($F(\xi, \eta)$, $S(\xi, \eta)$) and drags experienced at the surface $\left(Re^{1/2}C_f,\ Re^{1/2}\overline{C}_f\right)$. An increase in the yaw angle (θ) of the cylinder results in elevated fluid pressure, thus boosting the velocity in both orientations, as seen in Figures 13 and 14. However, the identical alterations of θ result in contrasting patterns in the gradients. Specifically, Figures 15 and 16 show a decrement of 96% and 75% approximately in for surging θ to 60° from 15° at $\xi = 1$ and $\varphi_3 = 0.02$. Additionally, Figures 13–16 compare the BHNF and THNF in terms of friction and velocity in the span and chord orientations. The THNF has lower velocity when compared to BHNF due to the collision of the extra component of the added nanoparticles, which in turn develops higher friction at the surface. Notably, a roughly 88% and 75% higher magnitude of friction is observed in for a THNF at $\xi = 1$ and $\theta = 45^0$.

4.4 Energy transfer rates of different fluids and shape effects of nanoparticles

The Nusselt number ($Re^{-1/2}Nu$), which characterizes how efficiently energy transfers in Figure 17, and is being used to compare Casson-Williamson (C-W) base fluid ($\varphi_1 = \varphi_2 = \varphi_3 = 0$), C-W nanofluid ($\varphi_1 = 0.02$, $\varphi_2 = \varphi_3 = 0$), C-W BHNF ($\varphi_1 = 0.02$, $\varphi_2 = 0.02$, $\varphi_3 = 0$) and C-W THNF ($\varphi_1 = 0.02$, $\varphi_2 = 0.02$, $\varphi_3 = 0.02$). Figure 16 shows that the C-W THNF is how efficient in heat transfer processes. The magnitude of $Re^{-1/2}Nu$ is higher for C-W THNF, followed by C-W BHNF, C-W nanofluid, and C-W base fluid. In particular, C-W THNF has 62% and 21% more $Re^{-1/2}Nu$ than the C-W base fluid and C-W BHNF at $\xi = 1$. The catalyst for this is the

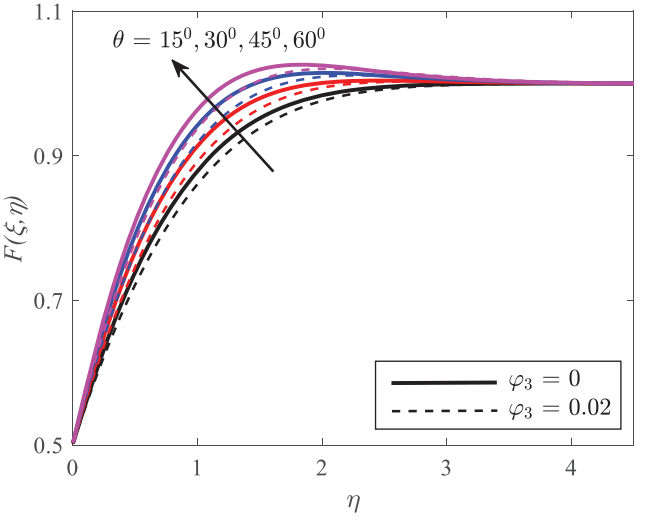

Source: Figure by authors

Figure 13. Impact of yaw angle (θ) and third component of the ternary hybrid nanofluid (φ_3) on the Chordwise velocity profile

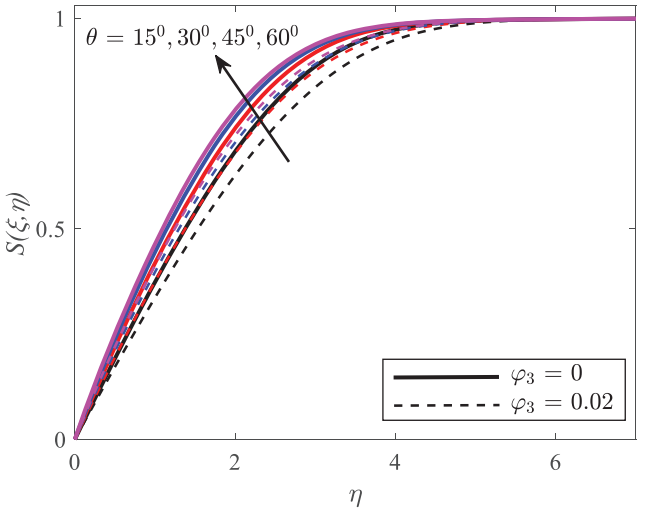

Source: Figure by authors

Figure 14. Impact of yaw angle (θ) and third component of the ternary hybrid nanofluid (φ_3) on the spanwise velocity profile

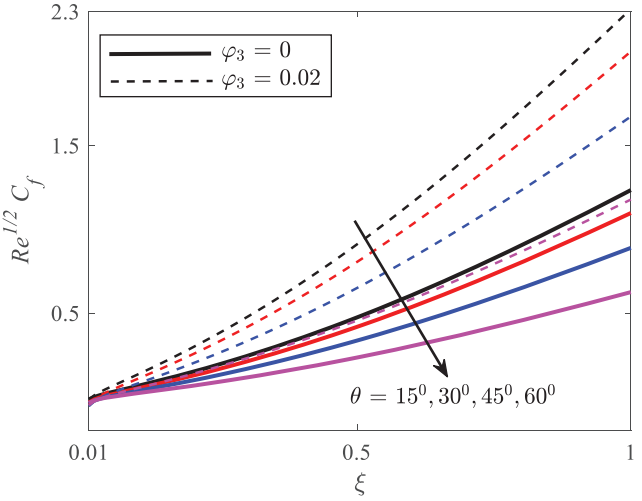

Source: Figure by authors

Figure 15. Impact of yaw angle (θ) and third component of the ternary hybrid nanofluid (φ_3) on the chordwise skin-friction coefficient

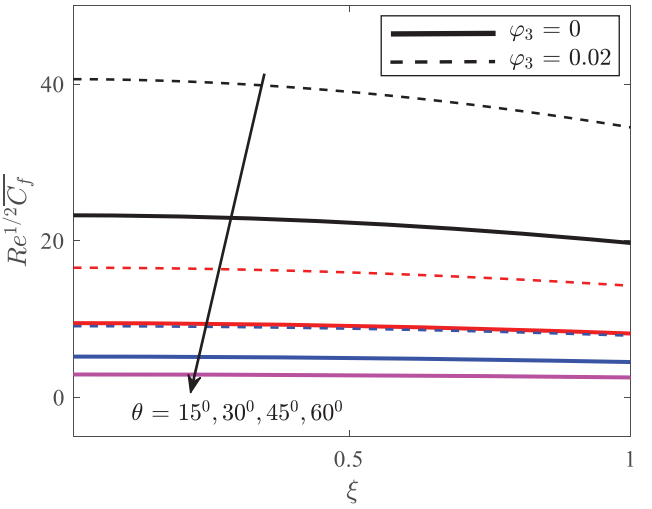

Source: Figure by authors

Figure 16. Impact of yaw angle (θ) and third component of the ternary hybrid nanofluid (φ_3) on the spanwise skin-friction coefficient

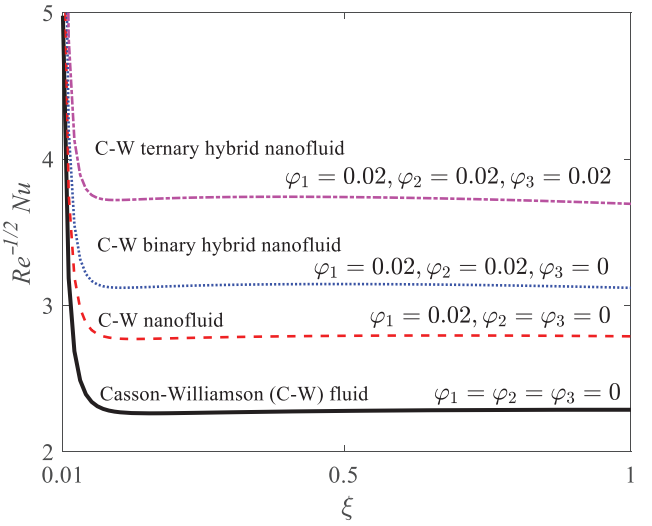

Source: Figure by authors

Figure 17. Energy transfer rate of different fluids (base fluid, nanofluid, bi-component and tri-component hybrid nanofluids)

fluid's nanoparticles, which boost the heat transmission efficiency. Thus, using C-W THNF is more energy-efficient in transferring energy than using single or bi-component nanofluids.

An essential factor in heat transfer procedures when dealing with nanoparticles is the shape of the nanoparticles. An instance of the impact of these shapes over $Re^{-1/2}Nu$ is displayed in Figure 18. Nanoparticles can be found in a wide variety of conformations, including spherical, columnar (cylindrical), tetrahedron, hexahedron, and lamina forms. The experimental values of the shape factors for each shape can be found in the literature, which can be used for theoretical computations. Knowing the nanoparticle's sphericity allows one to determine the shape factor s. The relationship between shape factors and sphericity is inverse, expressed by the equation $s = \frac{3}{\Omega}$, where Ω is the sphericity. The $Re^{-1/2}Nu$ is improved when the values of s evolve, meaning that altering the nanoparticles' shape from spherical to various forms improves the $Re^{-1/2}Nu$. Shortly, when the nanoparticles' morphologies were modified from spherical to laminar at $\xi = 1$, the $Re^{-1/2}Nu$ was increased by around 38%. In addition, Figure 19 illustrates the various shapes of the nanoparticles taken for the present work.

5. Conclusions

An effort is made herein to know the impression of Casson-Williamson THNF flow over a yawed cylinder under the influence of multiple slips and an inclined magnetic field. The whole study's observations are concluded below point-wise:

- As the Casson parameter is increased, we see an improvement in the velocity profiles in both orientations, while the gradients $Re^{1/2}C_f$, $Re^{1/2}\overline{C}_f$ reduce for the same variations of β.
- The velocities of Casson THNF are greater than those of Casson-Williamson THNF.

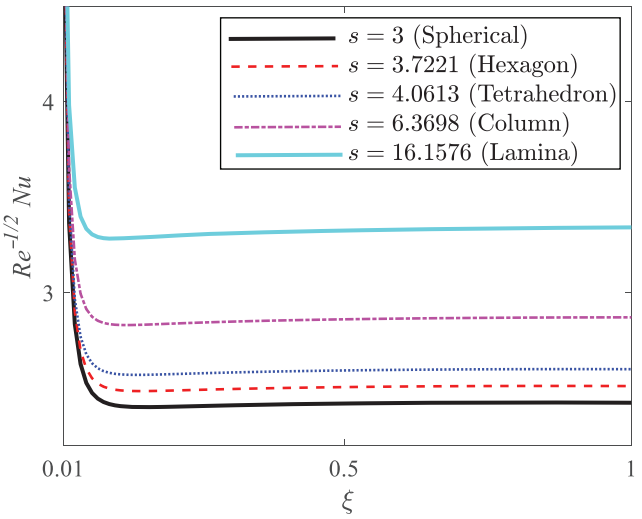

Source: Figure by authors

Figure 18. Energy transfer rate for different shapes of nanoparticles

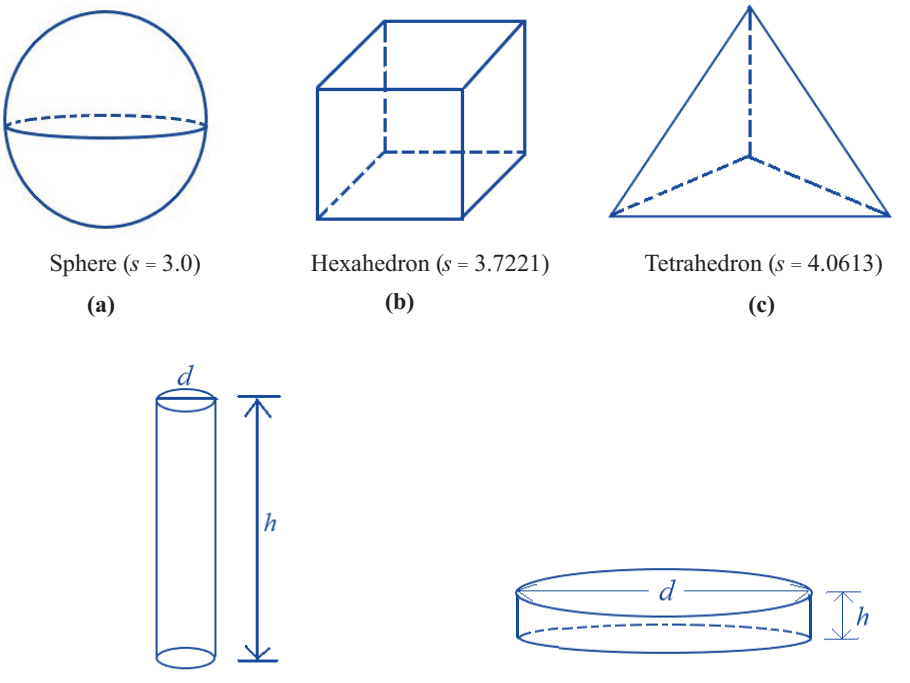

Sphere (s = 3.0) **(a)** | Hexahedron (s = 3.7221) **(b)** | Tetrahedron (s = 4.0613) **(c)**

Column (s = 6.3698) **(d)** | Lamina (s = 16.1576) **(e)**

Notes: (a) Sphere (s = 3.0); (b) hexahedron (s = 3.7221); (c) tetrahedron (s = 4.0613); (d) column (s = 6.3698); (e) lamina (s = 16.1576)
Source: Figure by authors

Figure 19. Shapes of nanoparticles

- The friction encountered on the surface of the yawed cylinder is higher when using Casson-Williamson THNF than when using Casson THNF alone. In particular, approximately a 202% and a 32% ascension are remarked in the magnitudes of $Re^{1/2}C_f$ and $Re^{1/2}\overline{C}_f$ for Casson-Williamson THNF than the Casson THNF only.
- Rising variations of M and α advance the $F(\xi, \eta)$, $G(\xi, \eta)$, the energy transport ability ($Re^{-1/2}Nu$) and hinders the growth of friction along Spanwise orientation.
- Selectively, a decline of approximately 82% and 72% in $Re^{1/2}C_f$ and $Re^{1/2}\overline{C}_f$ are noted while M emerges from 0 to 2 and α from 30° to 60° at $\xi = 1$.
- The THNF has lower velocity when compared to BHNF due to the collision of the extra component of the added nanoparticles, which in turn develops higher friction at the surface.
- The magnitude of ($Re^{-1/2}Nu$) is higher for C-W THNF, followed by C-W BHNF, C-W nanofluid, and C-W base fluid. In particular, C-W THNF has 62% and 21% more ($Re^{-1/2}Nu$) than the C-W base fluid and C-W BHNF at $\xi = 1$.

- Altering the nanoparticles' shape from spherical to various forms improves the ($Re^{-1/2}Nu$). Shortly, when the nanoparticles' morphologies were modified from spherical to laminar at $\xi = 1$, the ($Re^{-1/2}Nu$) was increased by around 38%.
- In future this work can be extended by including bioconvection and time-dependent (unsteady) nature of the flow regime.

References

Abbas, W., Megahed, A.M., Ibrahim, M.A. and Said, A.A.M. (2023), "Ohmic dissipation impact on flow of Casson-Williamson fluid over a slippery surface through a porous medium", *Indian Journal of Physics*, Vol. 97 No. 14, pp. 4277-4283. doi: 10.1007/s12648-023-02754-4.

Abdelhafez, M.A., Abd-Alla, A.M., Abo-Dahab, S.M. and Elmhedy, Y. (2023), "Influence of an inclined magnetic field and heat and mass transfer on the peristaltic flow of blood in an asymmetric channel", *Scientific Reports*, Vol. 13 No. 1, p. 5749.

Ahmad, B., Ahmad, M.O., Farman, M., Akgul, A. and Riaz, M.B. (2023), "A significance of multi slip condition for inclined MHD nanofluid flow with non-linear thermal radiations, dufour and soret, and chemically reactive bio-convection effect", *South African Journal of Chemical Engineering*, Vol. 43, pp. 135-145.

Akolade, M.T. and Tijani, Y.O. (2021), "A comparative study of three-dimensional flow of casson–williamson nanofluids past a Riga plate: spectral quasi-linearization approach", *Partial Differential Equations in Applied Mathematics*, Vol. 4, p. 100108.

Arshad, M., Alharbi, F.M., Hassan, A., Haider, Q., Alhushaybari, A., Eldin, S.M., Ahmad, Z., Al-Essa, L.A. and Galal, A.M. (2023), "Effect of inclined magnetic field on radiative heat and mass transfer in chemically reactive hybrid nanofluid flow due to dual stretching", *Scientific Reports*, Vol. 13 No. 1, p. 7828.

Asmat, F., Khan, W.A., Usman, Shamshuddin, M.D., Salawu, S.O. and Bouye, M. (2023), "Thermal analysis in an electrically conducting fluid with multiple slips and radiation along a plate: a case study of stokes' second problem", *Case Studies in Thermal Engineering*, Vol. 44, p. 102831.

Bellman, R.E. and Kalaba, R.E. (1965), *Quasilinearization and Nonlinear Boundary Value Problems*, Elsevier Publishing, New York, NY.

Benkhedda, M., Boufendi, T. and Touahri, S. (2018), "Laminar mixed convective heat transfer enhancement by using Ag-TiO2-water hybrid nanofluid in a heated horizontal annulus", *Heat and Mass Transfer*, Vol. 54 No. 9, pp. 2799-2814.

Bhuvaneswari, M., Sivasankaran, S., Niranjan, H. and Eswaramoorthi, S. (2019), "Cross diffusion effects on MHD convection of Casson-Williamson fluid over a stretching surface with radiation and chemical reaction", *Applied Mathematics and Computation, in Trends in Mathematics*, doi: 10.1007/978-3-030-01123-9_15.

Chiu, W.S. and Lienhard, J.H. (1967), "On real fluid flow over yawed circular cylinders", *Journal of Basic Engineering*, Vol. 89 No. 4, pp. 851-857.

Gray, D.D. and Giorgini, A. (1976), "The validity of boussinesq approximation for liquids and gases", *International Journal of Heat and Mass Transfer*, Vol. 19 No. 5, pp. 545-551.

Gul, T. and Saeed, A. (2022), "Nonlinear mixed convection couple stress trihybrid nanofluids flow in a Darcy–Forchheimer porous medium over a nonlinear stretching surface", *Waves in Random and Complex Media*, doi: 10.1080/17455030.2022.2077471.

Gupta, T.R. and Sarma, G.N. (1975), "Effect of cross-flow in unsteady flow past a yawed infinite cylinder", *Indian Journal of Pure and Applied Mathematics*, Vol. 6, pp. 1047-1065.

Hayat, T., Asghar, S., Tanveer, A. and Alsaedi, A. (2017), "Outcome of slip features on the peristaltic flow of a Prandtl nanofluid with inclined magnetic field and chemical reaction", *The European Physical Journal Plus*, Vol. 132 No. 5, p. 217.

Humane, P.P., Patil, V.S. and Patil, A.B. (2021), "Chemical reaction and thermal radiation effects on magnetohydrodynamics flow of Casson–Williamson nanofluid over a porous stretching surface", *Proceedings of the Institution of Mechanical Engineers, Part E: Journal of Process Mechanical Engineering*, Vol. 235 No. 6, pp. 2008-2018.

Inouye, K. and Tate, A. (1974), "Finite difference version of quasilinearization applied to boundary layer equations", *AIAA Journal*, Vol. 12 No. 4, pp. 558-560.

Jenifer, A.S., Saikrishnan, P. and Rajakumar, J. (2021), "Steady MHD flow over a yawed cylinder with mass transfer", *Frontiers in Heat and Mass Transfer*, Vol. 17 No. 0, pp. 1-8.

Khan, U., Zaib, A. and Ishak, A. (2021), "Non-similarity solutions of radiative stagnation point flow of a hybrid nanofluid through a yawed cylinder with mixed convection", *Alexandria Engineering Journal*, Vol. 60 No. 6, pp. 5297-5309.

Kumar, P., Nagaraj, B., Almeida, F., Ajaykumar, A.R., Al-Mdallal, Q. and Jarad, F. (2023a), "Magnetic dipole effects on unsteady flow of Casson-Williamson nanofluid propelled by stretching slippery curved melting sheet with buoyancy force", *Scientific Reports*, Vol. 13 No. 1, p. 12770.

Kumar, P., Poonia, H., Ali, L., Shah, N.A. and Chung, J.D. (2023b), "Significance of weissenberg number, Soret effect and multiple slips on the dynamic of biconvective magnetohydrodynamic carreau nanofluid flow", *Mathematics*, Vol. 11 No. 7, p. 1685.

Manjunatha, S., Puneeth, V., Gireesha, B.J. and Chamkha, A.J. (2022), "Theoretical study of convective heat transfer in ternary nanofluid flowing past a stretching sheet", *Journal of Applied and Computational Mechanics*, Vol. 8 No. 4, pp. 1279-1286.

Nandeppanavar, M.M., Raveendra, N. and Kemparaju, M.C. (2023), "Computational study of consequence of effect of velocity slip on nanofluids with suspended CNTs", *Numerical Heat Transfer; Part A: Applications*, Vol. 84 No. 12, pp. 1537-1551.

Nazir, U., Sohail, M., Hafeez, M.B. and Krawcjuk, M. (2021), "Significant production of thermal energy in partially ionized hyperbolic tangent material based on ternary hybrid nanomaterials", *Energies*, Vol. 14 No. 21, p. 6911.

Oke, A.S. (2022), "Heat and mass transfer in 3D MHD flow of EG-based ternary hybrid nanofluid over a rotating surface", *Arabian Journal for Science and Engineering*, Vol. 47 No. 12, pp. 16015-16031.

Patil, P.M. (2008), "Effects of free convection on the oscillatory flow of a polar fluid through a porous medium in the presence of variable wall heat flux", *Journal of Engineering Physics and Thermophysics*, Vol. 81 No. 5, pp. 905-922.

Patil, P.M., Kumbarwadi, N. and Shashikant, A. (2010), "Effects of MHD mixed convection with non-uniform heat source/sink and cross-diffusion over exponentially stretching sheet", *International Journal of Heat and Mass Transfer*, Vol. 53 Nos 21/22, pp. 4741-4748.

Patil, P.M., Roy, S. and Pop, I. (2013), "Chemical reaction effects on unsteady mixed convection boundary layer flow past a permeable slender vertical cylinder due to a nonlinearly stretching velocity", *Chemical Engineering Communications*, Vol. 200 No. 3, pp. 398-417.

Patil, P.M., Benawadi, S. and Shanker, B. (2022), "Influence of mixed convection nanofluid flow over a rotating sphere in the presence of diffusion of liquid hydrogen and ammonia", *Mathematics and Computers in Simulation*, Vol. 194, pp. 764-781.

Patil, P.M., Goudar, B. and Momoniat, E. (2023a), "Magnetized bioconvective micropolar nanofluid flow over a wedge in the presence of oxytactic microorganisms", *Case Studies in Thermal Engineering*, Vol. 49, p. 103284.

Patil, P.M., Goudar, B. and Sheremet, M.A. (2023b), "Tangent hyperbolic ternary hybrid nanofluid flow over a rough-yawed cylinder due to impulsive motion", *Journal of Taibah University Science*, Vol. 17 No. 1, p. 2199664.

Patil, P.M., Roy, M., Shashikant, A., Roy, S. and Momoniat, E. (2018), "Triple diffusive mixed convection from an exponentially decreasing mainstream velocity", *International Journal of Heat and Mass Transfer*, Vol. 124, pp. 298-306.

Patil, P.M., Doddagoudar, S.H., Hiremath, P.S. and Momoniat, E. (2019a), "Influence of applied magnetic field on mixed convective nanofluid flow past an exponentially stretching surface with roughness", *Journal of the Brazilian Society of Mechanical Sciences and Engineering*, Vol. 41 No. 12, p. 562.

Patil, P.M., Shashikant, A. and Hiremath, P.S. (2019b), "Effects of surface roughness on mixed convection nanoliquid flow over slender cylinder with liquid hydrogen diffusion", *International Journal of Hydrogen Energy*, Vol. 44 No. 21, pp. 11121-11133.

Priyanka, P., Abdelmohsen, S., A., M., Tawade, J.V., Ashraf, A., M.M., Kumar, R. and Biradar, M.M. (2023), "Multiple slip effects of MHD boundary-layer motion of a casson nanoliquid over a penetrable linearly stretching sheet embedded in non-Darcian porous medium", *International Journal of Modern Physics B*, Vol. 37 No. 3, p. 2350022.

Radbill, R.J. and McCue, A.G. (1970), *Quasilinearization and Nonlinear Problems in Fluid and Orbital Mechanics*, Elsevier Publishing Co, New York, NY.

Roy, S. and Anilkumar, D. (2006), "Unsteady mixed convection from a moving vertical slender cylinder", *Journal of Heat Transfer*, Vol. 128 No. 4, pp. 368-373.

Schlichting, H. and Gersten, K. (2000), *Boundary Layer Theory*, Springer, New York, NY.

Srinivasulu, T. and Goud, B.S. (2021), "Effect of inclined magnetic field on flow, heat, and mass transfer of Williamson nanofluid over a stretching sheet", *Case Studies in Thermal Engineering*, Vol. 23, p. 100819.

Takhar, H.S., Chamkha, A.J. and Nath, G. (2000), "Combined heat and mass transfer along a vertical moving cylinder with a free stream", *Heat and Mass Transfer*, Vol. 36 No. 3, pp. 237-246.

Thapa, J., Zhao, M., Zhou, T. and Cheng, L. (2014), "Three-dimensional simulation of vortex shedding flow in the wake of a yawed circular near a plane boundary at a Reynolds number of 500", *Ocean Engineering*, Vol. 87, pp. 25-39.

Xu, H. (2019), "Modelling unsteady mixed convection of a nanofluid suspended with multiple kinds of nanoparticles between two rotating disks by generalized hybrid model", *International Communications in Heat and Mass Transfer*, Vol. 108, p. 104275.

Yousef, N.S., Megahed, A.M., Ghoneim, N.I., Elsafi, M. and Fares, E. (2022), "Chemical reaction impact on MHD dissipative Casson-Williamson nanofluid flow over a slippery stretching sheet through porous medium", *Alexandria Engineering Journal*, Vol. 61 No. 12, pp. 10161-10170.

Further reading

Patil, P.M. and Shankar, H.F. (2022), "Heat transfer attributes of Al2O3-Fe3O4/H2O hybrid nanofluid flow over a yawed cylinder", *Propulsion and Power Research*, Vol. 11 No. 3, pp. 416-429.

Corresponding author

Ebrahim Momoniat can be contacted at: emomoniat@uj.ac.za